Synthesis of bis chromene derivative as a dual-functional corrosion inhibitor and CDK2 targeting agent

S.A. Saoud,[1] S.A. Habeeb,[1] M.I. Ali[2] and H.A. Almashhadani[2]*

[1]Department of Chemistry, College of Education for pure science (Ibn Al-Haitham), University of Baghdad, Baghdad 61023, Iraq
[2]Department of chemistry, College of Science, University of Baghdad, Baghdad, Iraq
**E-mail: H_R200690@yahoo.com*

Abstract

(*N*′[1]*Z*,*N*′[6]*Z*)-*N*′[1],*N*′[6]-Bis(2-(3,4-dihydroxyphenyl)-3,5,7-trihydroxy-4*H*-chromen-4-ylidene)-adipohydrazide was synthesized and characterized using nuclear magnetic resonance ([1]H-NMR, [13]C-NMR) and Fourier Transform Infrared spectroscopy (FTIR). The synthesis of chromene derivatives has garnered significant interest due to their wide range of biological activities and applications in medicinal chemistry, particularly pharmaceuticals. The current study highlights recent advancements in chromene derivatives and their role in the corrosion inhibition of carbon steel (CS), which was studied using electrochemical polarization techniques and electrochemical impedance spectroscopy (EIS) in a saline solution (3.5% NaCl) and an inhibited saline solution containing 200 ppm of the inhibitor over a temperature range of 303–323 K. The highest inhibition efficiency (*IE*%) of the synthesized inhibitor was 95.26% at 303 K. An atomic force microscope (AFM) was used to examine the surface morphology of the CS in both free and inhibited solutions. Kinetic and thermodynamic parameters of the transition state, including the apparent activation energy (E_a*), pre-exponential factor (*A*), activation enthalpy (Δ*H**), activation entropy (Δ*S**), and Gibbs free energy of activation (Δ*G**), were estimated. Additionally, a significant portion of the study explores molecular docking with CDK2 and includes comparisons to anticancer drugs. The prepared compound showed potential as a drug for breast cancer, although further studies are required to validate its efficacy.

Received: April 5, 2025. Published: June 12, 2025 doi: 10.17675/2305-6894-2025-14-2-25

Keywords: *quercetin, adipohydrazide, chromene, corrosion inhibitor, carbon steel, molecular docking.*

1. Introduction

Acid hydrazide derivatives are chemical compounds synthesized by modifying hydrazine hydrate, a highly reactive and toxic molecule. Their development has become essential with advancements in science. These compounds are considered important in many industries, including agriculture and healthcare.

Drug development is a priority in modern scientific research across many industrial fields in general, and in pharmaceutical chemistry in particular. One scientific approach involves the production of numerous synthetic chromene derivatives, followed by analysis

of the relationship between chemical structure, physical activity, and biological activity, in order to identify the most effective drug candidates. The synthesis of chromene derivatives has attracted significant interest due to their wide range of biological activities and applications in medicinal chemistry (pharmaceuticals), materials science, physics and organic electronics. Therefore, our research efforts focus on finding new synthetic chromene derivatives with unique physical properties, which are becoming an area of growing interest in both pharmaceutical and chemical compounds. Various chromene derivatives have demonstrated anti-breast cancer [1], anti-inflammatory [2], antibacterial [3], antiviral [4], antioxidant properties [5], as well as activity in molecular docking studies [6]. The use of several chromene derivatives to enhance melanin production in the skin has also been demonstrated. Based on the available literature, there are multiple methods for preparing chromene from its raw materials. One such method described in this research involves the reaction of quercetin, a ketone compound, with adipohydrazide. In this context, the search for simple, efficient and inexpensive reaction systems for synthesizing new chromene derivatives and evaluating their physical and biological properties represents an important area of research. Recent studies have focused on studying this class of compounds within organic chemistry, especially regarding their biological and physical applications.

As a result, the current study provides an overview of recent advancements in the application of quercetin derivatives to enhance the surface properties of various metals, especially in relation to corrosion inhibition. Metals and their alloys undergo significant corrosion when exposed to sodium chloride solutions [7]. Corrosion is an undesirable and destructive process for materials caused by the effects of corrosive environments on materials [8]. One of the easiest ways to prevent corrosion is to use a corrosion inhibitor. Chemically active organic compounds containing heteroatoms and/or π-electrons, as well as certain inorganic compounds, are commonly used as corrosion inhibitors [9]. Numerous organic compounds have been found effective in preventing metal corrosion in aggressive solutions. Chromene, a compound with delocalized electrons, heteroatoms, and polar functional groups, demonstrate these corrosion-inhibiting properties [9]. This effectiveness is ascribed to the formation of chemical and/or physical bonds between the metallic surface and molecules with high electron density, leading to the development of a protective, corrosion-resistant layer [10–13]. Moreover, molecular docking technology has been used to predict interactions between molecules and to evaluate the potential use of these compounds as drugs by studying the bonding between the proteins and the resulting molecules [14–16].

In this study, (*N*′^{1}*Z*,*N*′^{6}*Z*)-*N*′^{1},*N*′^{6}-bis(2-(3,4-dihydroxyphenyl)-3,5,7-trihydroxy-4*H*-chromen-4-ylidene)adipohydrazide was synthesized and characterized using nuclear magnetic resonance (^{1}H-NMR, ^{13}C-NMR), Fourier Transform Infrared (FTIR) spectroscopy. Also, its efficacy as a corrosion inhibitor for carbon steel (hereafter CS) in a 3.5% NaCl solution was investigated within the temperature range of 303–323 K through docking studies. The surface morphology of CS was examined using atomic force microscopy (AFM) in both the free and inhibitor solutions.

2. Experimental Part

2.1. Synthesis of (N′¹Z,N′⁶Z)-N′¹,N′⁶-bis(2-(3,4-dihydroxyphenyl)-3,5,7-trihydroxy-4H-chromen-4-ylidene)adipohydrazide

Saoud *et al*. [17] converted an acid into an ester using benzene sulfonic acid (BSA). Then, acid hydrazide (adipohydrazide) was synthesized from the corresponding ester in the presence of hydrazine hydrate [8]. Finally, a solution of quercetin (0.2 mol) in 20 mL of absolute ethanol was prepared, and adipohydrazide (0.1 mol) was added gradually in small portions. Then, acetic acid was added as a catalyst. The mixture was then refluxed for 11–12 hours. After cooling, the precipitate was filtered and washed with cold ethanol. The desired product was purified by flash column chromatography using ethyl acetate: hexane [6:1] as the eluent, yielding a yellow precipitate with a 78% yield and a melting point (m.p.) of 268–270°C. IR (KBr, U_{max}/cm^{-1}), (3400−3180) cm^{-1} OH, (3049–3014) cm^{-1} CH-aromatic, (2972−2885) cm^{-1} CH-aliphatic, 1650 cm^{-1} (C=O) amid, 1600 cm^{-1} (C=N), (1583−1400) cm^{-1} C=C; ^{1}H NMR (400 MHz, DMSO-d_6) δ, ppm; 1.38 (t, 4H, $COCH_2CH_2$), 1.82 (t, 4H, $COCH_2CH_2$), 4.85 (bs, 8H, OH), 6.55 (s, 2H, CH-aromatic), 6.94 (s, 2H, CH-aromatic), 7.08 (s, 2H, CH-aromatic), 7.08–8.29 (m, 4H, CH-aromatic), 9.54 (bs, 2H, NH), 11.58 (bs, 2H, OH); ^{13}C NMR (75 MHz, DMSO-d6) δ, ppm; 29.72 (2C, $COCH_2CH_2$), 37.72 (2C, $COCH_2CH_2$), 101.87 (2C, CH-aromatic), 109.69 (2C, CH-aromatic), 110.70 (2C, CH-aromatic), 118.64 (2C, CH-aromatic), 121.45 (2C, CH-aromatic), 125.39 (2C, CH-aromatic), 128.52 (2C, C), 148.84 (2C, C–OH), 151.98 (2C, C–OH), 154.23 (2C, C−OH), 155.89 (2C, C), 156.78 (2C, C),159.50 (2C, C=N), 163.14 (2C, C–OH), 163.77 (2C, C−OH), 167.80 (2C, C=O).

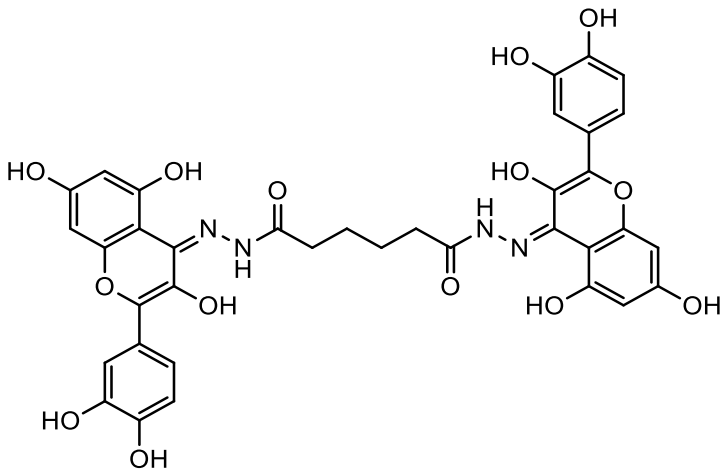

(*N*′¹*Z*,*N*′⁶*Z*)-*N*′¹,*N*′⁶-bis(2-(3,4-dihydroxyphenyl)-3,5,7-trihydroxy-4*H*-chromen-4-ylidene)adipohydrazide

Figure 1. Chemical structure of chromene derivative.

2.2. Metal sample

This study was carried out using the CS, with its composition detailed in Table 1.

Table 1. Chemical composition of CS.

	C%	Si%	Mn%	S%	P%	Cu%	Ni%	Cr%	Fe%
Carbon steel	0.36–0.42	0.15–0.30	1.00–1.40	0.05	0.05	0.50	0.20	0.20	96.88–97.49

2.3. Electrochemical techniques

2.3.1. Electrochemical polarization technique

The electrochemical polarization technique utilizes a cell in which three electrodes are immersed in a corrosive solution (3.5% NaCl). These electrodes include the working electrode (CS), the reference electrode (saturated calomel electrode (SCE)) and the auxiliary electrode (platinum electrode). All corrosion parameters were evaluated for CS in both uninhibited and inhibited 3.5% NaCl solutions containing 200 ppm of the synthesized inhibitor over a temperature range of 303–333 K. In this method, the corrosive solution (3.5% NaCl) was first added to the corrosion cell. The reference electrode was then filled with the same corrosive solution, followed by insertion of the CS into the working electrode holder to measure its corrosion rate. Then the OCP was determined. The corrosion current density was subsequently measured by using a potentiostat apparatus, where the potential was measured as a function of current. This was achieved by analyzing the current-potential data using the potentiostat software.

2.3.2. Electrochemical impedance spectroscopy (EIS)

Electrochemical impedance spectroscopy (EIS) is one of the most effective techniques for determining the resistivity of corrosion products, electrolyte solutions, or materials in electrochemical systems. CS was evaluated in both uninhibited and inhibited 3.5% NaCl solutions containing 200 ppm of the synthesized inhibitor over a temperature range of 303–333 K. The impedance test was conducted after allowing the sample to stabilize until its potential became constant. The test employed a saturated calomel electrode (SCE) as the reference electrode, CS as the working electrode, and platinum as the auxiliary electrode. Also, the impedance test was undertaken with a 10 mV amplitude at the frequency range of 0.01 to 1 MHz.

2.4. Atomic Force Microscope (AFM)

Atomic Force microscopy (AFM) imaging of an insulated structure at atomic resolution involves a cantilever with a sharp tip (probe) at its end, which is used to scan the surface of the specimen. Scanning is a dynamic process, and since the tip is in mechanical contact with

the surface of the CS, the attractive force between the tip and the surface is detected. This attractive force arises from van der Waals interactions between the surface and the tip [18].

2.5. Molecular Docking

2.5.1 Computational details

Avogadro software [19] was used to build and optimize the structures of the prepared molecules and drugs. When molecular docking was required, molecular files were converted to the Structure Data File (SDF) format using the Open Babel software [20]. Protein structures were obtained from the NCBI database in PDB format, and then cleaned and prepared using AutoDock4 [21]. The preparation process involved the removal of existing inhibitors and water molecules, as well as structural repair and optimization.

For the docking process, the protein was uploaded in PDB format, while the ligand molecules (inhibitor, drug, or the prepared compound) were uploaded in SDF format to the CB-Dock2 website [22]. The docking process started with a cavity search, followed by selecting the desired cavity, where the docking calculations were performed. CB-Dock2, ChimeraX [23] and Autodock4 were used to visualize and analyze the molecular docking results.

3. Results and Discussion

3.1. Characterization of (N′¹Z,N′⁶Z)-N′¹,N′⁶-bis(2-(3,4-dihydroxyphenyl)-3,5,7-trihydroxy-4H-chromen-4-ylidene)adipohydrazide

Esterification was carried out by reacting adipic acid with absolute ethanol, which also acted as the solvent, in the presence of benzenesulfonic acid (BSA). Subsequently, acid hydrazide was synthesized from the corresponding ester using a normal hydrazination process. Finally, the hydrazide was reacted with quercetin in ethanol to yield the desired hydrazide (Schiff base) in high yield [24, 25]. The sequence of these step is illustrated in Scheme (1).

The collected data were consistent with the proposed structure. The IR spectra exhibited a new signal for the imine group (C=N) at 1600 cm^{-1}, while the carbonyl group of the hydrazones appeared at 1650 cm^{-1}. In the ^{1}H NMR spectrum, the compound showed the disappearance of the NH_2 peak, while a new peak appeared at 9.54 ppm due to NH. The hydroxyl group adjacent to the C=N moiety appeared as a broad signal at 11.58 ppm, while another OH group was observed at 4.85 ppm. Moreover, two distinct CH_2 groups appeared, *i.e.*, the CH_2 group adjacent to C=O appeared at 1.82 ppm due to four protons and the other CH_2 group appeared at 1.38 ppm due to four protons.

The ^{13}C NMR spectra displayed new carbons of aromatic from quercetin, along with a distinct peak from adipohydrazide. The signals at 29.72 ppm and 37.72 ppm were assigned to the CH_2 groups- one adjacent to C=O and the other adjacent to another CH_2 group. The aromatic carbon signals were observed in the range of 101.87–128.52 ppm, while carbons bearing hydroxyl groups appeared in the range of 148.84–154.23 ppm. Moreover, two characteristics signals at 159.50 ppm and 167.80 ppm were attributed to the C=N and C=O groups, respectively.

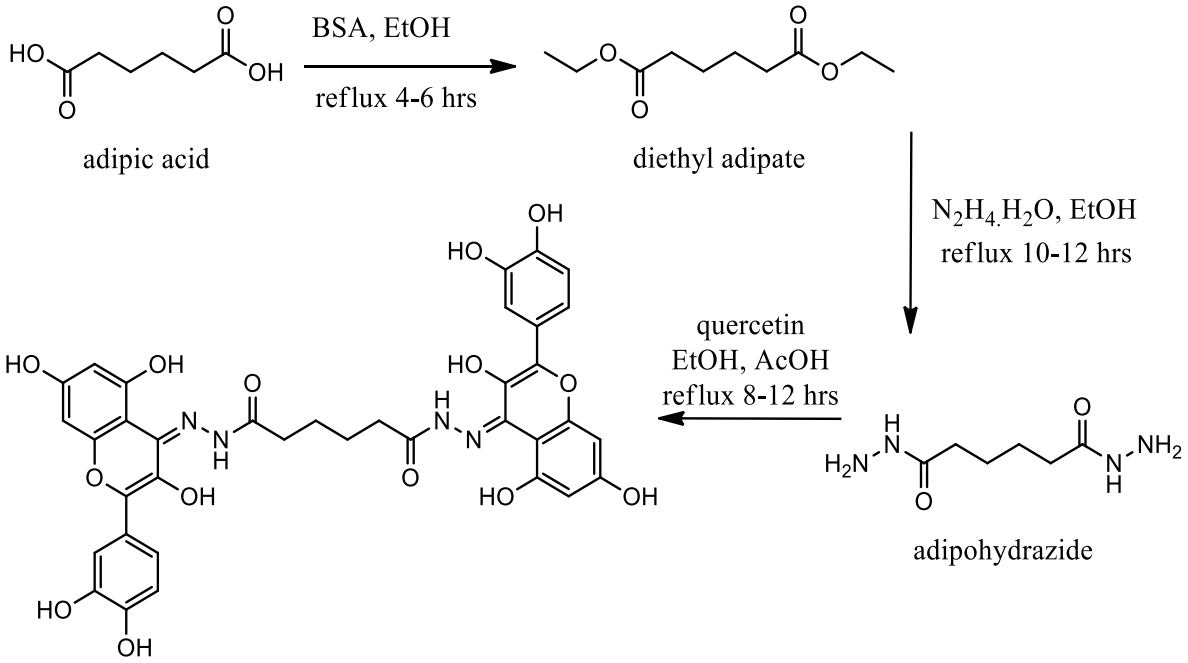

Scheme 1. Synthesis route of (*N*′¹*Z*,*N*′⁶*Z*)-*N*′¹,*N*′⁶-bis(2-(3,4-dihydroxyphenyl)-3,5,7-trihydroxy-4*H*-chromen-4-ylidene)adipohydrazide.

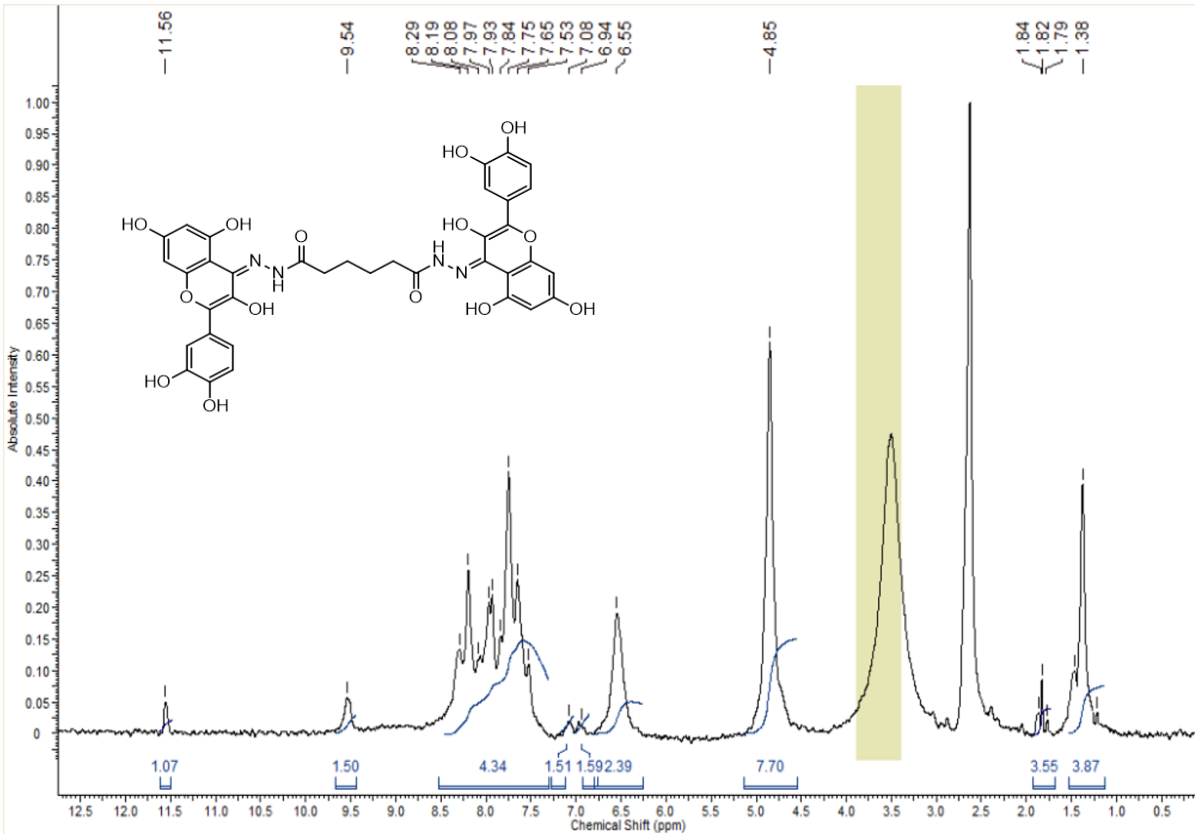

Figure 2. ¹H-NMR of (*N*′¹*Z*,*N*′⁶*Z*)-*N*′¹,*N*′⁶-bis(2-(3,4-dihydroxyphenyl)-3,5,7-trihydroxy-4*H*-chromen-4-ylidene)adipohydrazide.

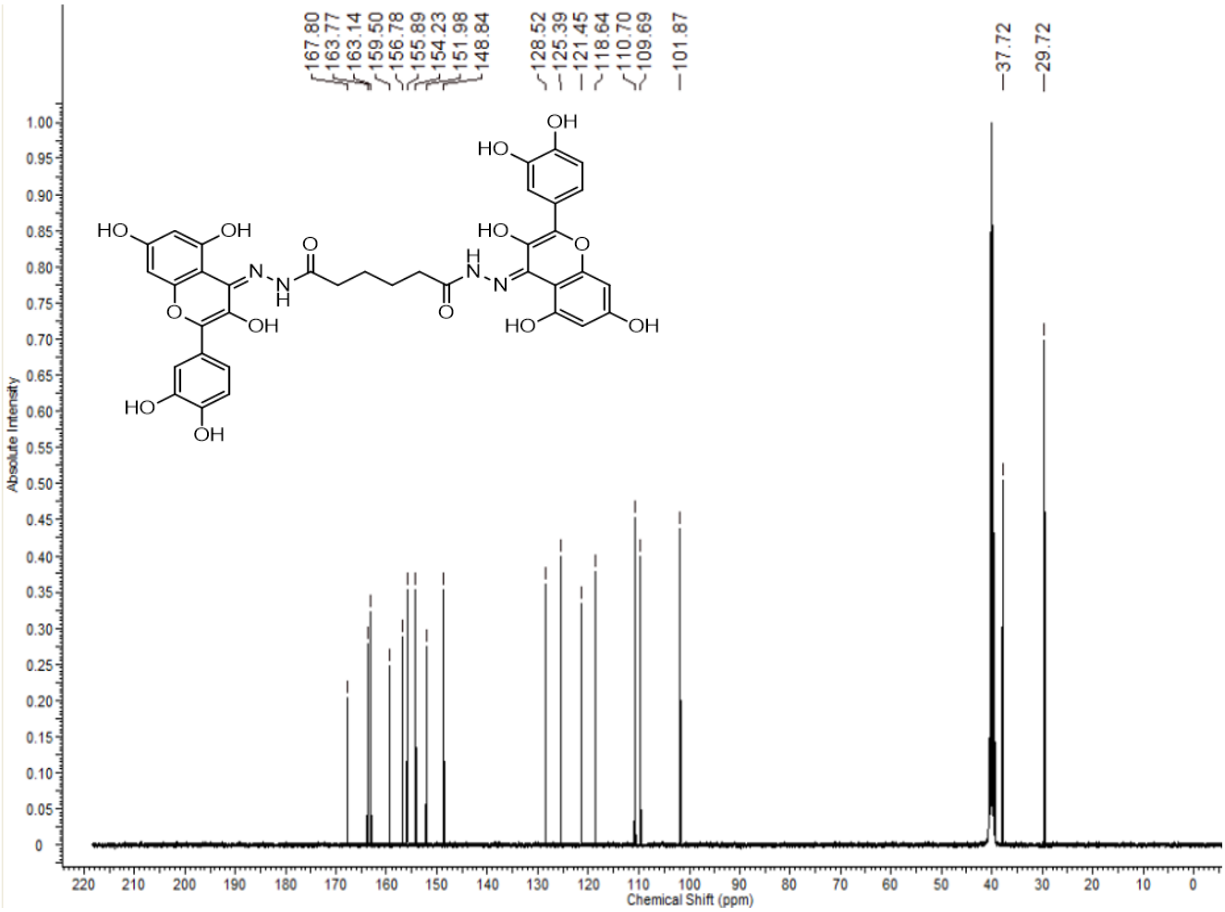

Figure 3. ^{13}C-NMR of (*N*′^{1}*Z*,*N*′^{6}*Z*)-*N*′^{1},*N*′^{6}-bis(2-(3,4-dihydroxyphenyl)-3,5,7-trihydroxy-4*H*-chromen-4-ylidene)adipohydrazide.

3.2. Corrosion parameters

The corrosion parameters were determined based on the data presented in Table 2 and Figure 4. The corrosion potential (E_{corr}) and corrosion current density (i_{corr}) were determined by extrapolating the cathodic and anodic Tafel lines to their intersection point for CS in both uninhibited and inhibited solutions. The cathodic (β_c) and anodic (β_a) Tafel slopes were calculated form the potentiodynamic polarization curves shown in Figure 4. Table 2 presents the values of E_{corr} (mV), i_{corr} (mA/cm^2), anodic (β_a) and cathodic Tafel slopes (β_c) (mV/Dec), polarization resistance (R_p) (Ω/cm^2) and inhibition efficiency (*IE*%). The *IE*% values were calculated as follows [26]:

$$IE\% = \frac{(i_{corr})_0 - (i_{corr})}{(i_{corr})_0} \times 100\,, \qquad (1)$$

where $(i_{corr})_0$ and (i_{corr}) are the corrosion current density for CS in the absence and presence of the inhibitor, respectively.

Table 2. Corrosion parameters for CS in blank (3.5%NaCl) and inhibitor (200 ppm) solutions at temperature range 303–323 K.

Sample	T (K)	$-E_{corr}$ (mV)	i_{corr} (mA/cm^2)	β_c (mV/dec)	β_a (mV/dec)	R_p (Ω/cm^2)	IE%
Blank (3.5%NaCl)	303	671.3	0.0876	148	94	284.4	–
	313	739.7	0.1242	221	103	244.8	–
	323	510.6	0.1292	216	84	202.7	–
	333	649.4	0.1817	111	110	163.7	–
200 ppm (inhibitor)	303	533.2	0.0042	152	104	6458	95.26
	313	658.4	0.0108	320	335	6604	91.33
	323	641.1	0.0121	190	233	3778	90.66
	333	835.7	0.0263	72	67	835.7	85.55

Based on the analysis of the curves in Figure 4 and the electrochemical parameters in Table 2, it can be observed that the corrosion rate increases when rising temperature in both uninhibited and inhibited solutions. Nevertheless, after the saline solution is inhibited by chromene, there is a reduction in corrosion current densities. Based on the data presented in Figure 4, there is no clear trend in corrosion potential with increasing temperature. Table 2 shows the anodic (β_a) and cathodic (β_c) Tafel slopes, which were determined from their respective Tafel regions. At all temperatures, the values of anodic and cathodic Tafel slope (β_a and β_c) exhibit variation. In the cathodic reaction, these variations are attributed to changes in the rate-determining step, shifting from the charge transfer to electrochemical desorption or chemical deposition. Similarly, changes in the rate-determining step are also observed in the metal dissolution reaction [27, 28]. At 303 K, the *IE*% of the inhibitor (chromene derivative) reaches 95.26%. This high efficiency can be attributed to the fact that these molecules have a rich electronic density since they contain heteroatoms, aromatic rings, and π-electrons. In fact, this density facilitates the adsorption of the inhibitor onto the metallic surface by forming inhibitor-Fe complexes, which protect its surface [16]. The polarization resistance (R_p) was calculated using the rearranged Stern-Geary equation [29]:

$$R_p = \frac{\beta_a \cdot \beta_c}{2.303(\beta_a + \beta_c) i_{corr}} \quad (2)$$

The R_p values increase in presence of the inhibitor due to the near-complete coverage of CS and due to the more conductivity of the bare metal [30].

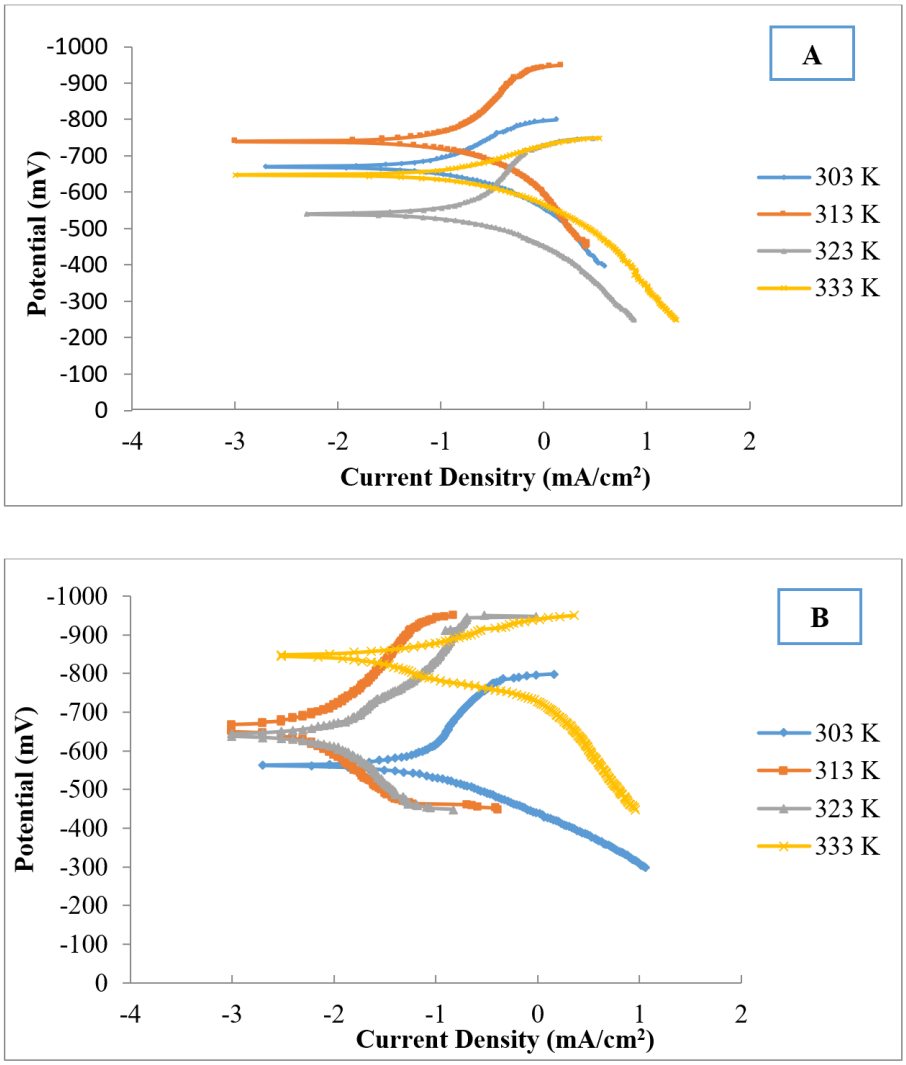

Figure 4. Tafel plot for CS in A) free solution, B) inhibitor solution at temperature range (303–333) K.

3.3. Mechanisms of corrosion inhibition

Chromene derivatives use a variety of complex mechanisms to prevent corrosion, which can be broadly classified into two main categories [31]. The first mechanism involves adsorption onto the surface of metals, forming a protective layer that acts as a barrier against corrosive agents. This adsorption process is influenced by factors such as the nature of the inhibitor, the type of metal, and the properties of the corrosive medium. The second mechanism involves the chemical transformation of the adsorbed inhibitors, leading to the formation of stable, protective layers, which function as barriers that prevent corrosive substances from penetrating the surface of metals, thereby slowing the electrochemical reactions that are responsible for corrosion.

3.4. Electrochemical impedance spectroscopy (EIS)

The corrosion behaviour of CS was evaluated in a 3.5% NaCl solution using the EIS, both in the absence and presence of the inhibitor. Figure 5 and Figure 6 show the typical impedance data in the form of Nyquist and Bode plots, respectively, whereas the equivalent circuit model is shown in Figure 7. Table 3 shows the equivalent circuit parameters, which include electrolyte resistance (R_1), pore resistance (R_2), charge transfer resistance (R_3), coating capacitance (C_1), double-layer capacitance (C_2) and inhibition efficiency (IE%). The inhibition efficiency was computed based on the charge transfer resistance as follows [32]:

$$IE\% = \frac{(R_{ct})_{inh} - (R_{ct})_0}{(R_{ct})_{inh}} \times 100, \quad (3)$$

where $(R_{ct})_{inh}$ and $(R_{ct})_0$ represent the charge transfer resistance in the presence and absence of the inhibitor, respectively.

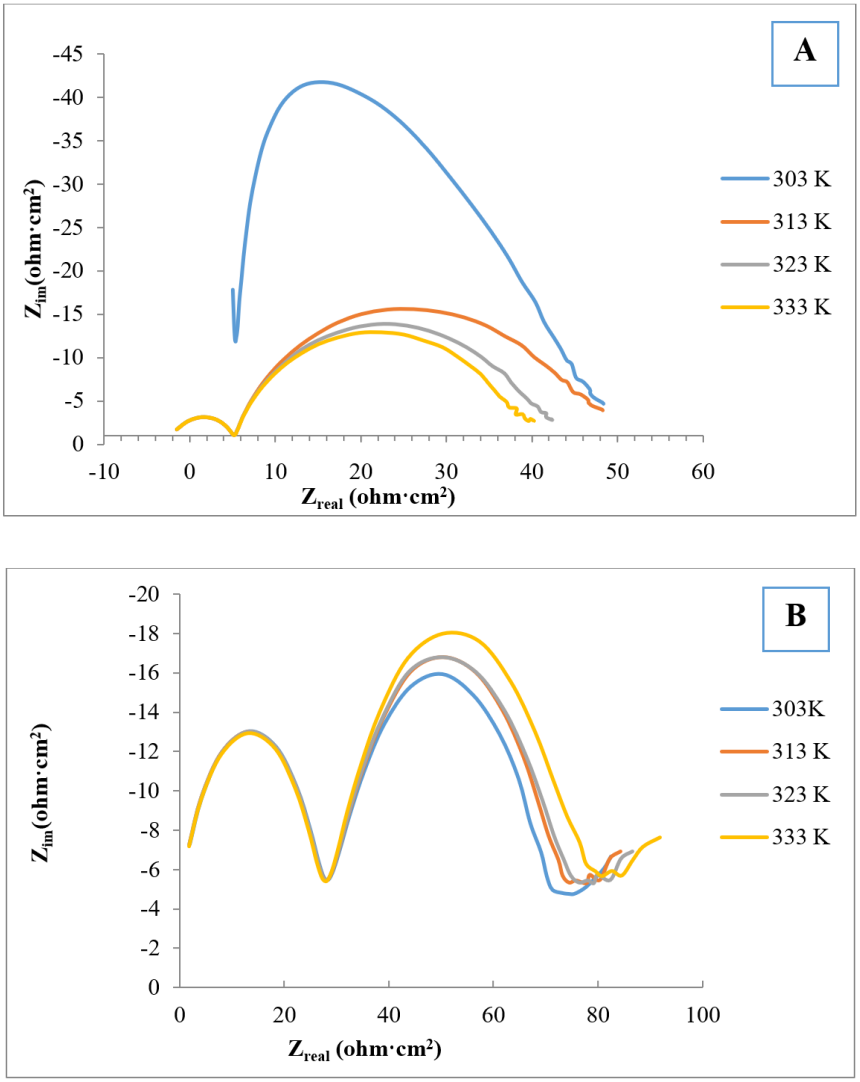

Figure 5. Nyquist plot for CS in A) free solution and B) inhibitor solution.

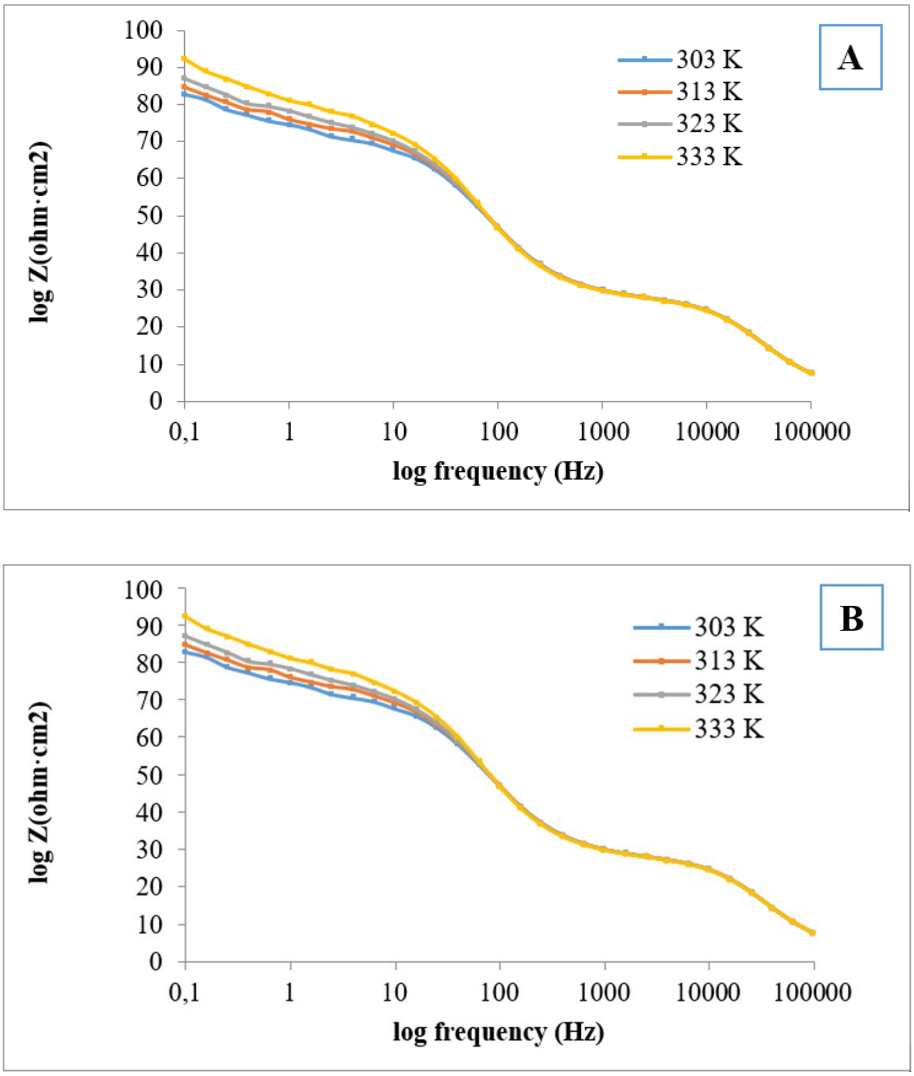

Figure 6. Bode plot for CS in A) free solution and B) inhibitor solution.

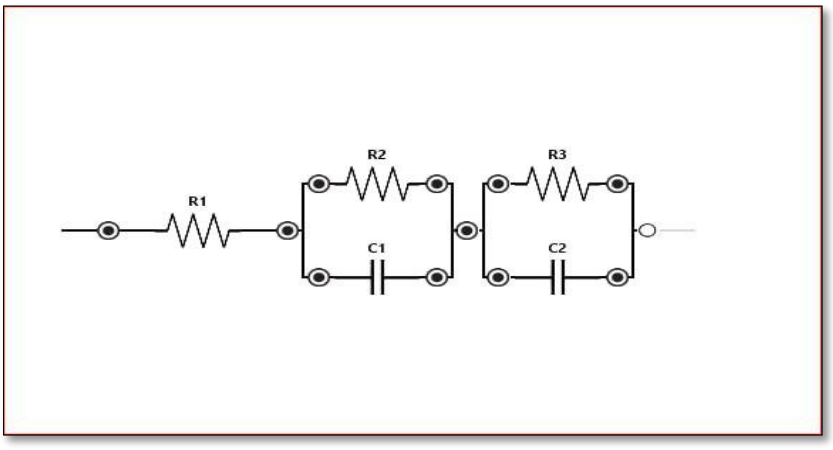

Figure 7. Equivalent circuit model used to fit EIS data.

Table 3. Electrochemical impedance parameters for CS in absence and presence of inhibitor over a temperature range of 303–333 K.

	***T* (K)**	***R*$_1$ (Ohm)**	***R*$_2$ (Ohm)**	***R*$_3$ (Ohm)**	***C*$_1$ (F)**	***C*$_2$ (F)**	***IE*%**
Blank	303 K	0.03055	37.08	5.892	$6.563 \cdot 10^{-4}$	$2.622 \cdot 10^{-6}$	–
	313 K	0.03100	35.82	6.371	$7.933 \cdot 10^{-4}$	$2.622 \cdot 10^{-6}$	–
	323 K	0.08234	32.55	5.882	$6.161 \cdot 10^{-4}$	$2.655 \cdot 10^{-6}$	–
	333 K	0.00087	29.69	6.738	$7.280 \cdot 10^{-4}$	$2.615 \cdot 10^{-6}$	–
Inhibitor	303 K	0.2837	49.20	28.26	$5.622 \cdot 10^{-5}$	$2.385 \cdot 10^{-7}$	79.151
	313 K	0.2865	45.92	28.39	$5.477 \cdot 10^{-5}$	$2.359 \cdot 10^{-7}$	77.559
	323 K	0.2914	44.49	28.29	$5.329 \cdot 10^{-5}$	$2.362 \cdot 10^{-7}$	79.208
	333 K	1.473	38.03	28.23	$5.993 \cdot 10^{-5}$	$2.801 \cdot 10^{-7}$	76.132

The results show that when the inhibitor is added, R_{ct} values increase. The adsorption of the inhibitor molecules on the surface of the CS results in an increase in the double-layer thickness, which lowers the double-layer capacitance (C_2) [33]. The similarity of the Nyquist loops indicates that the corrosion mechanism does not change, regardless of the presence of the inhibitor [34]. The values of *IE*% estimated from EIS decrease with increasing temperature, consistent with the trend observed in polarization measurements, except at 313 K, where the *IE*% reaches 79.208% [35]. The capacitive loops are not perfect semicircles due to the frequency dispersion caused by the surface roughness and homogeneities of the CS surface [32].

3.5. Atomic Force Microscopy (AFM)

An AFM study was undertaken to further investigate the surface morphology of CS, as shown in Figures 8a and 8b. Owing to the attack of chloride ions, the surface of CS in the uninhibited solution exhibits a rough structure with numerous ups and downs, with an average surface roughness of 145.7 nm (see Figure 8a). However, the presence of the inhibitor reduced the surface roughness to 61.85 nm, resulting in a smoother surface and indicating a slower corrosion rate (Figure 8b). These findings suggest that inhibition occurs due to the presence of the inhibitor molecules that adsorb onto the surface of CS [36].

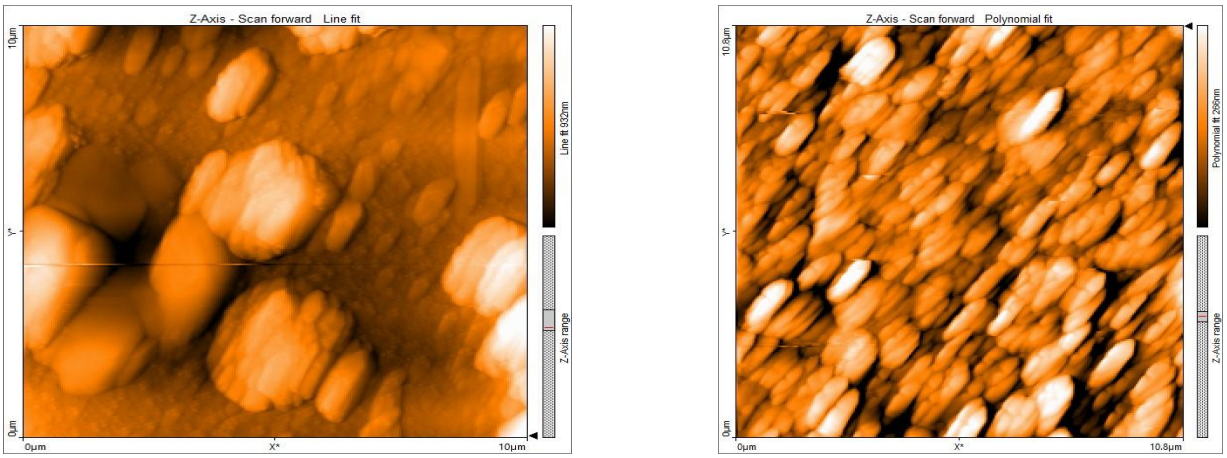

A **B**

Figure 8. AFM images for a) CS in a blank solution b) CS in an inhibitor solution.

3.6. Effect of temperature

The effect of temperature on the corrosion rate of CS in the absence and presence of the inhibitor was investigated over a temperature range of 303–333 K. Figure 9 was used to determine the activation energies by applying the Arrhenius equation [37].

$$\log i_{\text{corr}} = \log A - \frac{E_{\text{a}}}{2.303R} \tag{4}$$

Figure 10 was used to determine the activation entropy (ΔS^*) and activation enthalpy (ΔH^*) values for the corrosion of CS, both in the presence and absence of the inhibitor. The transition state equation was expressed as follows [38]:

$$\log \frac{i_{\text{corr}}}{T} = \log\left[\frac{R}{Nh} - \frac{\Delta S^*}{2.303R}\right] - \frac{\Delta H^*}{2.303RT} \tag{5}$$

In contrast, Gibbs equation [39] was used to estimate the activation free energies (ΔG^*).

$$\Delta G^* = \Delta H^* - T\Delta S \tag{6}$$

where E_{a} is the activation energy, R is the gas constant, A is the Arrhenius pre-exponential factor, T is the absolute temperature, h is the Plank constant and N is Avogadro's number. Table 4 presents all of the measured thermodynamic and kinetic parameters. The results indicate that the activation energy increases when the inhibitor is present, indicating the excellent inhibition efficiency of the synthetic inhibitor. The positive activation enthalpy (ΔH^*) values for CS, both in the absence and presence of the inhibitor, indicates an endothermic nature of the transition state process. The negative values of ΔS^* for CS in the absence and presence of the inhibitor show that the activation complexes in the rate-determining step represent an association rather than a dissociation, which imply a decrease in disorder as the system transitions from reactants to activated complexes [40, 41]. In addition, as the temperature increases, the positive values of ΔG^*, presented in Table 2, exhibit only minor changes.

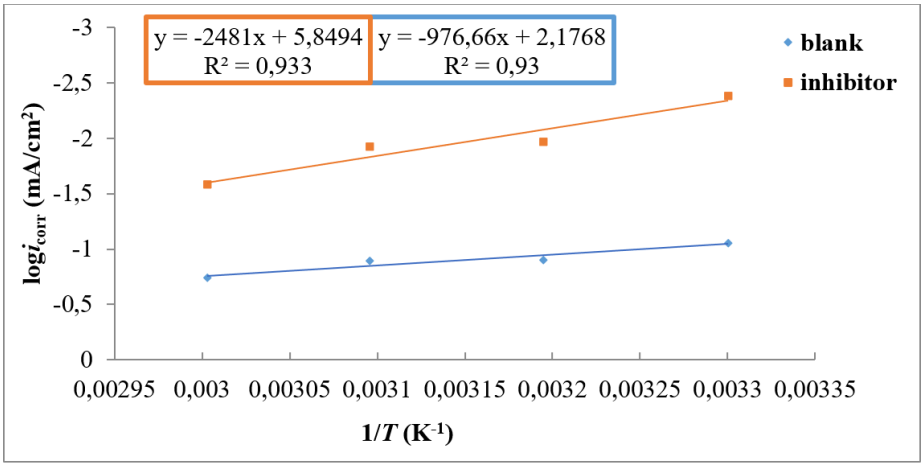

Figure 9. Arrhenius Plots of logi_{corr} against 1/T for CS in absence and presence of inhibitor.

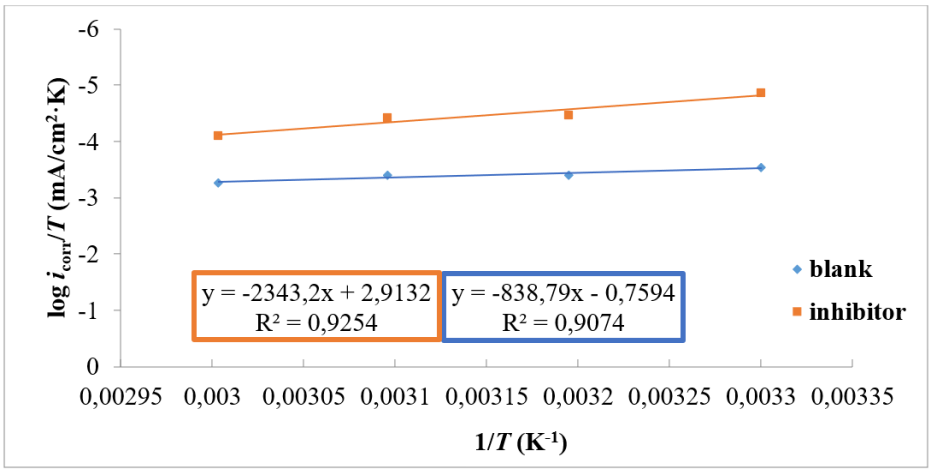

Figure 10. Plots of log i_{corr}/T against 1/T for CS in absence and presence of inhibitor.

Table 4. Kinetic and thermodynamic of activation parameters for CS in absence and presence of inhibitor at temperature range of 303–333 K.

	T **(K)**	***E*a** **(kJ/mol)**	***A*** **(molecule·cm²·s⁻¹)**	**Δ*H**** **kJ/mol**	**–Δ*S**** **J/mol·K**	**Δ*G**** **kJ/mol**
Blank	303	18.702	$5.2 \cdot 10^{24}$	16.0623	211.769	80.228
	313					82.346
	323					84.464
	333					86.581
Inhibitor	303	47.509	$4.3 \cdot 10^{29}$	44.871	141.449	42.904
	313					89.145
	323	47.509	$4.3 \cdot 10^{29}$	44.871	141.449	90.559
	333					91.974

3.7. Docking study

CDK2 is a member of the Cyclin-Dependent Kinase (CDK) family, a group of enzymes that regulate and control cell division in eukaryotic organisms. These enzymes are activated at specific stages of the cell cycle by binding to Cyclin proteins, in conjunction with ATP, to phosphorylate their target substrates [42, 43]. CDK2 has become a key target in research on anticancer drugs because of its essential role in cell cycle progression.

The human CDK2 enzyme, designated as 6OQI in the PDB database, consists of a single chain that contains 298 amino acids with the following sequence:

```
  0 FMENFQKVEKIGEGTYGVVYKARNKLTGEVVALKKIRLTAIREISLLKEL
 50 NHPNIVKLLDVIHTENKLYLVFEFLHQDLKKFMDASALTGIPLPLIKSYL
100 FQLLQGLAFCHSHRVLHRDLKPQNLLINTEGAIKLADFGLARAFGVPVRT
150 YTHEVVTLWYRAPEILLGCKYYSTAVDIWSLGCIFAEMVTRRALFPGDSE
200 IDQLFRIFRTLGTPDEVVWPGVTSMPDYKPSFPKWARQDFSKVVPPLDED
250 GRSLLSQMLHYDPNKRISAKAALAHPFFQDVTKPVPHLRL
```

Figure 11. Amino acid sequence that forms CDK2 chain.

The β-sheets of this enzyme are located in the first half of the beginning of its amino acid sequence, while the α-helixes are more predominant in the second half. The binding site of the ATP group, following the activation of the enzyme, is located in a deep gap on the surface of the protein between the beta sheets and the alpha helices.

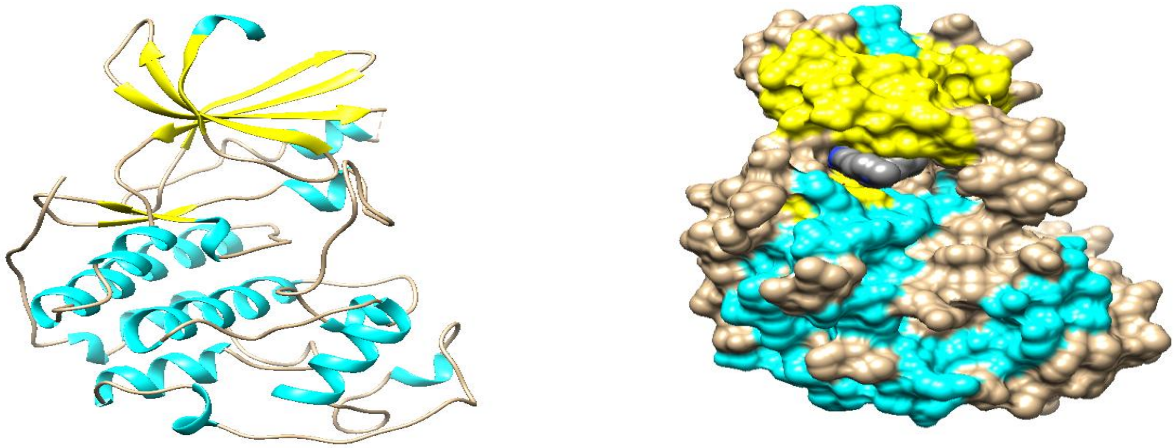

A **B**

Figure 12. (a) CDK2 active site location between β-Sheets zone and α-Helixes, (b) the active site occupied by N14 inhibitor obtained from X-ray crystal structure coded by 6OQI in PDB[44].

Cyclin protein binds to the other side of the active site on the enzyme surface after activation, as shown in the figure below:

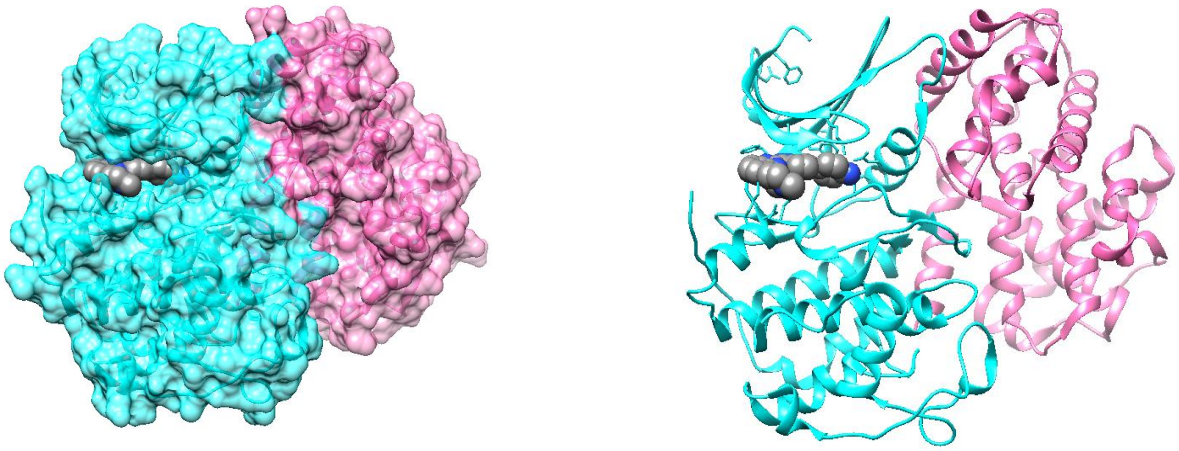

Figure 13. CDK2-complex with cyclin A with EZV inhibitor [45] which is coded by 3F5X in PDB database.

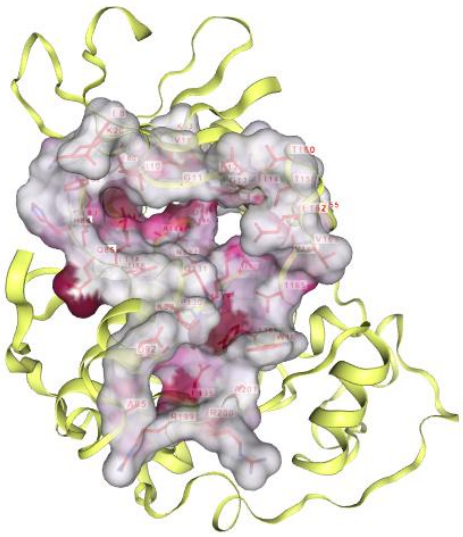

Figure 14. Active site cavity identified by CB-Dock2.

The amino acid segments within the active site that participate in molecular interactions with the ATP group or its competing inhibitors are as follows:

```
Query   0.........10.........20.........30.........50.........60.........70.........80.........90.........100.........110.....
A       FMENFQKVEKI GEGTYGVVYK ARNKLTGEVV ALKKIRLTAIR EISLLKELNH PNIVKLLDVI HTENKLYLVF EFLHQDLKKF MDASALTGIP  LPLIKSYLFQ  LLQGLA
        ...120.........130.........140.........150.........160.........170.........180.........190.........200.........210.......
        FCHS  HRVLHRDLKP  QNLLINTEGA  IKLADFGLAR  AFGVPVRTYT  HEVVTLWYRA  PEILLGCKYY  STAVDIWSLG  CIFAEMVTRR  ALFPGDSEID  QLFRIFR
        ..220.........230.........240.........250.........260.........270.........280.........290........
        TLG  TPDEVVWPGV  TSMPDYKPSF  PKWARQDFSK  VVPPLDEDGR  SLLSQMLHYD  PNKRISAKAA  LAHPFFQDVT  KPVPHLRL
```

Figure 15. Amino-acid segments included in the active site by CB-Dock2.

In addition to this active site pocket, two other allosteric active sites on the CDK2 surface affect the tertiary structure of the enzyme by binding to ligands [46]. These allosteric sites are not included in this study and will be the focus of future research.

CDK2 + Molc.

The prepared molecule interacts strongly with CDK2 by fitting into the active site cavity, showing a remarkable Vina score of –10.2 kcal/mole. The amino acid segments affected by this interaction were:

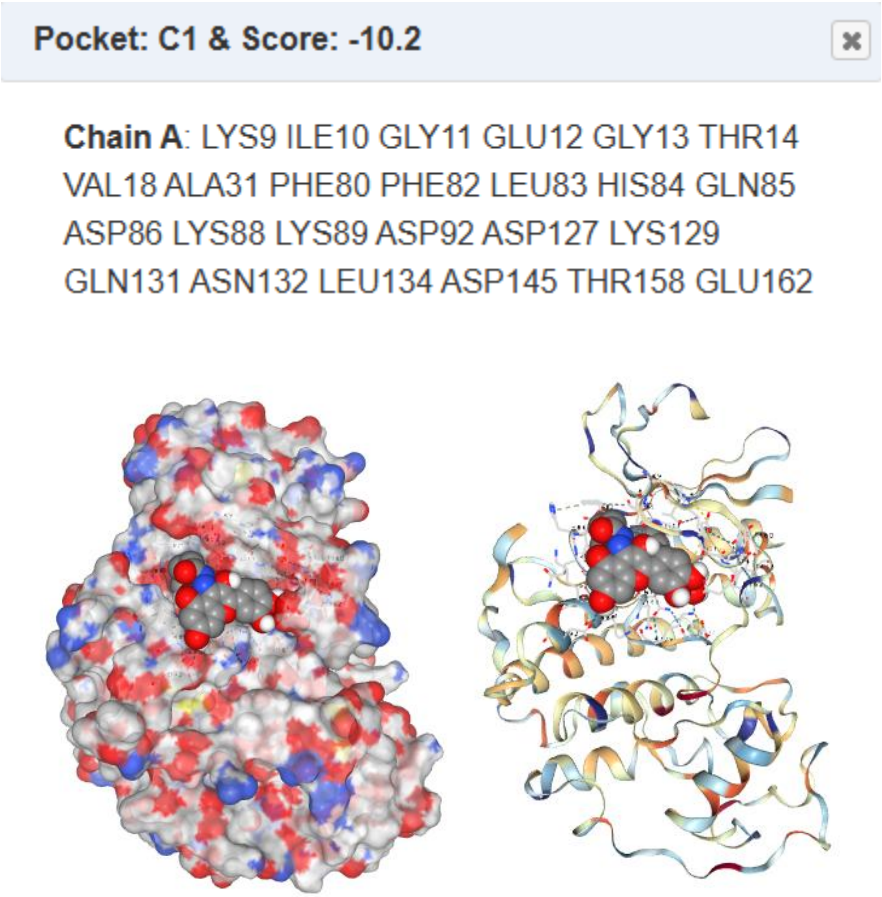

Figure 16. Global view of the CDK2-Molc. Docking complex.

This interaction is mainly hydrophobic in nature, dominated by Van der Waals and dipole-dipole interactions, along with some characteristic hydrogen bonding, which differs from that observed in other studies [47, 48] that focused on hydrogen bonding interactions with Glu81 and Leu83. The two catecholyl side groups are oriented in the same direction, allowing the hydrogen bonding with the amino group of Lys129, while the other interacts with Glu12 and Glu162. One of the coumarin groups, which lies adjacent to the external portion of the protein cavity, interacts strongly with Asp92 and Ile10 through hydrogen bonding. However, the other coumarin group, located deep inside the cavity, does not form any hydrogen bonding.

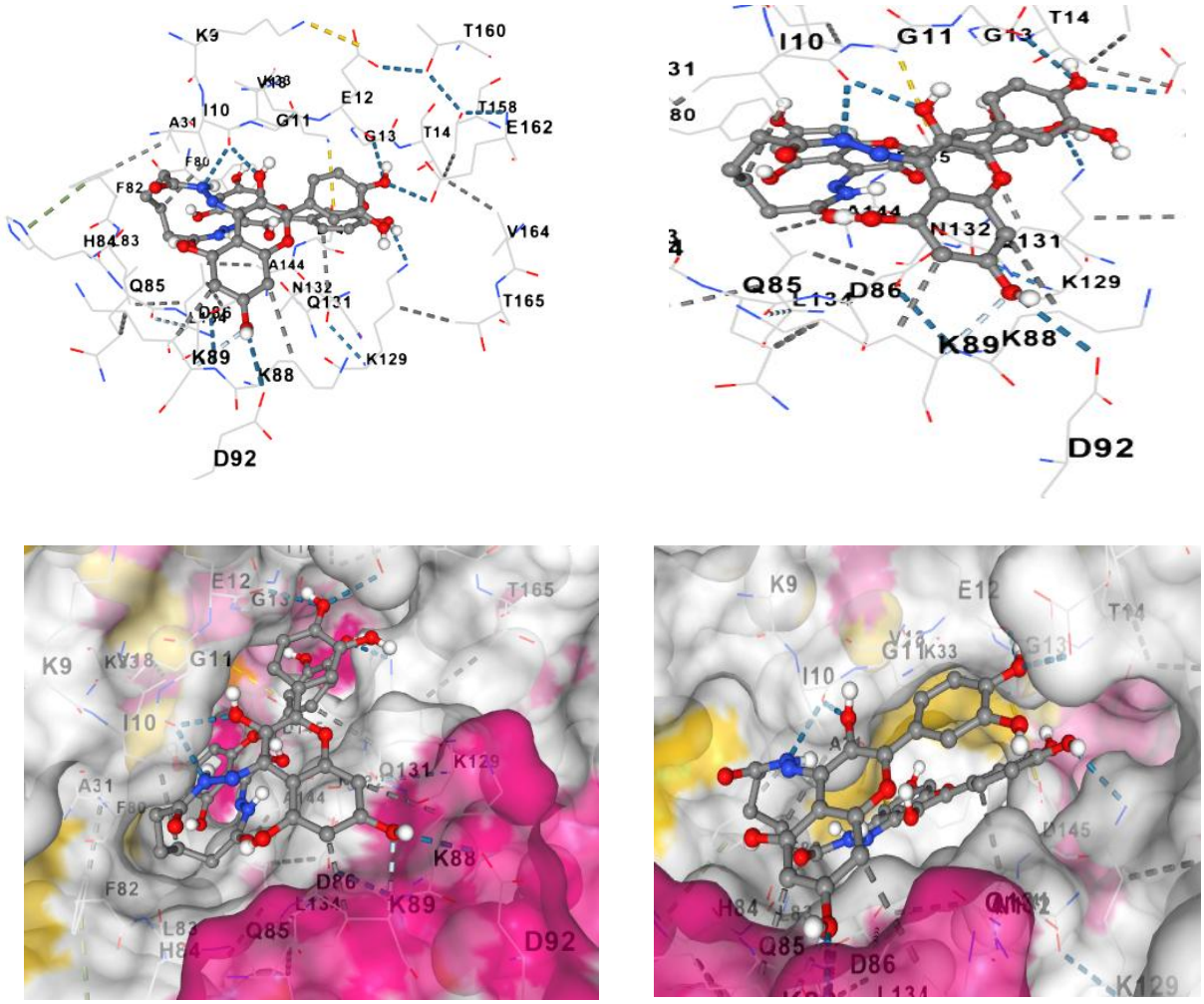

Figure 17. Detailed 3D interaction graph of the CDK2-Molc. Docking complex.

As mentioned above, the hydrogen bonding pattern of the studied compound within the ATP-competitive cavity is different from those in previous studies, but it has considerable binding affinity, which may enhance the specificity and selectivity of the compound.

Moreover, the water bridges observed in the X-ray-crystallographic complex structure of the N14 inhibitor with CDK2 (PDB:6OQI) were not considered in this study. Further investigation using solvated MD simulations of the docking complex is required to explore their potential role in binding interactions [49].

To extrapolate the anti-cancer activity of the prepared compound, molecular docking studies were undertaken using two FDA-approved breast cancer inhibitor drugs, namely Palbociclib with an IC50 of 15 nM [47], and Falvopiridol, with an IC50 of 100 nM [50]. Both drugs were docked into the same binding cavity of CDK2 under conditions similar to those used for the prepared compound. The Vina score values were –10.0 kcal/mole for Palbociclib and –9.6 kcal/mole for Flavopiridol, compared to –10.2 kcal/mole for the studied molecule. These results show that the compound has promising anti-cancer potential and merits further research.

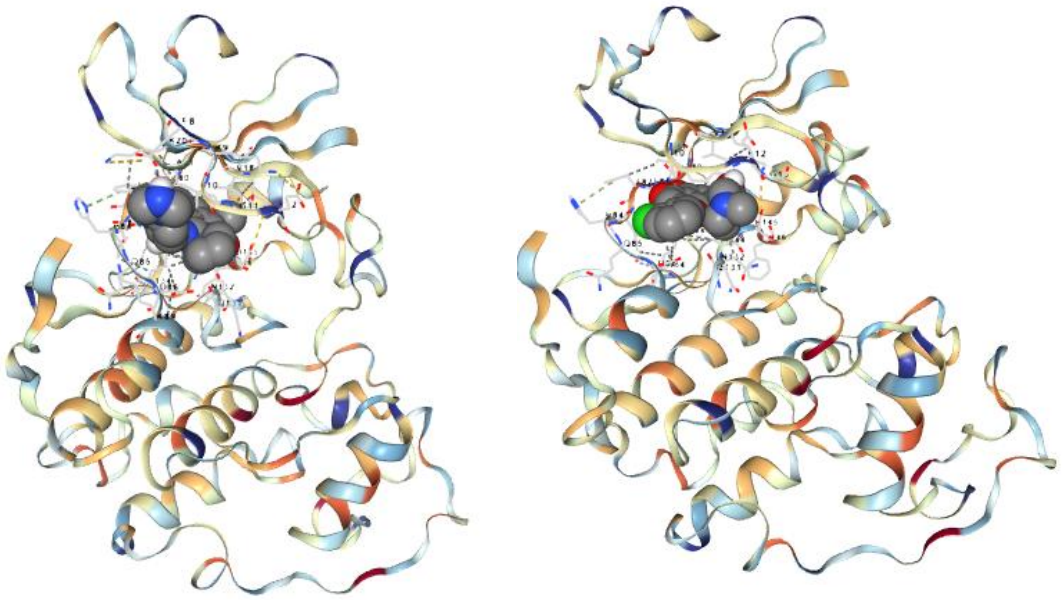

A **B**

Figure 18. Docking of FDA-approved anti-cancer drugs (A) Palbociclib, (B) Falvopiridol.

Table 5. DG of tested molecules against Falvopiridol and Palbociclib.

Ligand	RMSD value (Å)	Docking score (kcal/mol)	Interactions	
			H. B	Pi-interactions
Compound 1	1.50	–8.81	4	16
Falvopiridol	0.18	–9.65	4	8
Palbociclib	0.96	–9.69	4	9

4. Conclusions

Within the current study, Schiff bases were synthesized *via* the condensation reaction between acid hydrazide (adipohydrazide) and quercetin. This reaction required an acid catalyst (acetic acid) and refluxing for 11–12 hours to facilitate the removal of water molecules. The synthesized product was characterized using FT IR, ^{1}H NMR and ^{13}C NMR spectra, providing detailed insights into its structure. Moreover, the chemical structure was explored via molecular docking studies.

In a 3.5% NaCl solution, the examined chromene derivative exhibited excellent inhibition efficiency for CS. The polarization study indicated that the chromene derivative inhibitor acts as a mixed-type inhibitor. EIS analysis demonstrated that the inhibition occurs due to the adsorption of the chromene derivative molecules onto the surface of CS, resulting in a reduction in double-layer capacitance (C_2) and an increase in the charge transfer

resistance (R_3). Additionally, AFM images demonstrated that the inhibitor molecules form a protective layer on the surface of CS, protecting the surface against corrosive ions.

The increase in the E_a values in the presence of the inhibitor indicated an increase in the energy barrier for the corrosion reaction, which showed effective inhibition. Also, the positive values of ΔH^* showed the endothermic nature of the transition state in the corrosion reaction.

In conclusion, it should be noted that chromene derivative exhibits both anti-corrosion properties and biological activity, showing potential for use as a drug for breast cancer.

Acknowledgment

We would like to express our gratitude to the University of Baghdad, College of Education for Pure Science Ibn-AL-Haitham, for supporting this work. Also, we would like to extend our thanks to Abdulrahman Mohammed A. Saleh (Faculty of pharmacy for boys – Al-Azhar University, Cairo – Egypt, abdo.saleh240@gmail.com) for his valuable contribution to the molecular docking simulation study.

Conflicts of interest

The authors declare there are no conflicts of interest. All authors alone are accountable for the content and writing of the paper.

Funding

Self-funding.

Authorship contributions

All authors mention in this paper have done all requirements of this work.

References

1. A. Karimi, F. Naeini, V.A. Azar, M. Hasanzadeh, A. Ostadrahimi, H.R. Niazkar, M. Mobasseri and H. Tutunchi, A comprehensive systematic review of the therapeutic effects and mechanisms of action of quercetin in sepsis, *Phytomedicine*, 2021, **86**, 153567. doi: 10.1016/j.phymed.2021.153567
2. H.-S. Yoo, Y.-S. Yoon, J.-W. Shin, S.-I. Choi, S.H. Son, Y.H. Jang, Y.-S. Yang, S.-Y. Kim, Y.-R. Kim, K.-S. Chung, K.-T. Lee and N.-J. Kim, *In vitro* and *in vivo* anti-inflammatory and antinociceptive activities of a synthetic hydrangenol derivative: 5-hydroxy-2-(4-hydroxyphenyl)-4*H*-chromen-4-one, *Int. Immunopharmacol*., 2025, **148**, 114175. doi: https://doi.org/10.1016/j.intimp.2025.114175
3. E.M. Arzyamova and A.Y. Yegorova, Synthesis, crystal structure and evaluation of antibacterial activity of new hybrid systems containing furan-2-one and chromen-4-thione fragments, *Phosphorus, Sulfur, and Silicon and the Related Elements*, 2025, **200**, no. 2, 164–173. doi: 10.1080/10426507.2025.2461042

4. M.A. Kadhim, E.K.M. Zangana and A.H. Jawad, Design, synthesis and characterization of a new series of 2,3-dihydroquinazolin-4(1*H*)-one (DHQZ-1) derivatives and evaluation of antitumor resistant (by Molecule Docking), *Baghdad Sci. J.*, 2024, **21**, no. 7, 2263–2274. doi: 10.21123/bsj.2023.8232
5. H.Z. Jasim and H. Al-Shmgani, Cytotoxic potential activity of quercetin derivatives on MCF-7 breast cancer cell line, *Bionatura*, 2023, **8**, no. 1, 92. doi: 10.21931/RB/2023.08.01.92
6. Y. Wang, X. Cheng, X. Liu, J. Xu, L. Wang, S. Zhang, S. Liu and T. Peng, Design and Synthesis of 3-(2*H*-Chromen-3-yl)-5-aryl-1,2,4-oxadiazole Derivatives as Novel Toll-like Receptor 2/1 Agonists That Inhibit Lung Cancer *In Vitro* and *In Vivo*, *J. Med. Chem.*, 2024, **67**, no. 6, 4583–4602. doi: 10.1021/acs.jmedchem.3c01984
7. K. Li, C. Huang, P. Qi, L. Han, Q. Ye and Y. Li, High quantum yield blue fluorescent molecule of hydroxybenzo[c]chromen-6-ones: Synthesis and fluorescence characteristics, *J. Mol. Struct.*, 2025, **1321**, 139962. doi: 10.1016/j.molstruc.2024.139962
8. D. Roy, L. Haque, S. Das, A. Chakraborty and R. Ghosh, Metal ion sensing ability and photo-physical properties of 4-hydroxy-3-nitroso-2*H*-chromen-2-one: Interaction studies with calf thymus-DNA, *J. Lumin.*, 2019, **206**, 474–485. doi: 10.1016/j.jlumin.2018.10.102
9. A. Laarioui, I. Chaouki, A. Hmada, A.El Magri, N. Errahmany, F.El Hajri, N. Dkhireche, S.El Bakkali, R. Touir and S. Boukhris, Corrosion Inhibition Influence of the Synthetized Chromen-6-One Derivatives on Mild Steel in 1.0 M HCl Electrolyte: Electrochemical, Spectroscopic and Theoretical Investigations, *Mor. J. Chem.*, 2024, **12**, no. 2, 570–593. doi: 10.48317/IMIST.PRSM/morjchem-v12i2.45771
10. D. Douche, H. Elmsellem, E.H. Anouar, L. Guo, B. Hafez, B. Tüzün, A.E. Louzi, K. Bougrin, K. Karrouchi and B. Himmi, Anti-corrosion performance of 8-hydroxyquinoline derivatives for mild steel in acidic medium: Gravimetric, electrochemical, DFT and molecular dynamics simulation investigations, *J. Mol. Liq.*, 2020, **308**, 113042. doi: 10.1016/j.molliq.2020.113042
11. P.K. Paul, V. Saraswat and M. Yadav, Chromenes as efficient corrosion inhibitor for mild steel in HCl solution, *J. Adhes. Sci. Technol.*, 2019, **33**, no. 12, 1275–1293. doi: 10.1080/01694243.2019.1591774
12. Y. Youssefi, L. Oucheikh, O. Ou-ani, M. Jabha, A. Oubair, M. Znini, E.E. Ebenso and B. Hammouti, Synthesis, Characterization and Corrosion Inhibition Potential of Olefin Derivatives for Carbon Steel in 1 M HCl: Electrochemical and DFT Investigations, *Mor. J. Chem.*, 2023, **11**, no. 1, 155–187. doi: 10.48317/IMIST.PRSM/morjchem-v11i1.37306
13. A.N. Jasim, B.A. Abdulhussein, S.M.N. Ahmed, W.K. Al-Azzawi, M.M. Hanoon, M.K. Abbass and A.A. Al-Amiery, Schiff's Base Performance in Preventing Corrosion on Mild Steel in Acidic Conditions, *Prog. Color, Color. Coat.*, 2023, **16**, 319–329. doi: 10.30509/pccc.2023.167081.1197

14. M. Abouchane, N. Dkhireche, M. Rbaa, F. Benhiba, M. Ouakki, M. Galai, B. Lakhrissi, A. Zarrouk and M.E. Touhami, Insight into the corrosion inhibition performance of two quinoline3-carboxylate derivatives as highly efficient inhibitors for mild steel in acidic medium: Experimental and theoretical evaluations, *J. Mol. Liq*., 2022, **360**, 119470. doi: 10.1016/j.molliq.2022.119470
15. H. Zarrok, A. Zarrouk, R. Salghi and H. Oudda, Gravimetric and quantum chemical studies of 1-[4-acetyl-2-(4-chlorophenyl)quinoxalin-1(4*H*)-yl]acetone as corrosion inhibitor for carbon steel in hydrochloric acid solution, *J. Chem. Pharmac. Res*., 2012, **4**, no. 12, 5056–5066.
16. N. Öztürk, G. Celik, C. Alaşalvar, E. Temel and H. Gökçe, Synthesis, structural, spectroscopic (NMR, FT-IR and UV–Vis), NLO, in silico (ADMET and molecular docking) and DFT investigations of a flavonol derivative 2-(4-chlorophenyl)-7-fluoro-3-hydroxy-4*H*-chromen-4-one, *J. Mol. Struct*., 2025, **1322**, 140490. doi: 10.2139/ssrn.4847582
17. A. Ahmed, I. Majeed, N. Asaad, R. Ahmed, G. Kamil and S.A. Rahman, Some 3,4,5-trisubstituted-1,2,4-triazole synthesis, antimicrobial activity, and molecular docking studies, *Egyptian J. Chem*., 2022, **65**, no. 3, 395–401. doi. 10.21608/ejchem.2021.93025.4397
18. H.A. Salim and S.A. Saoud, Synthesis, Characterization, Antimicrobial Activity, and Docking Study of Some 1,3,4-Oxadiazole Derivatives with Tert-Amine Moiety, *Iran. J. Chem. Chem. Eng*., 2024, **43**, no. 9, 3221–3236. doi: 10.30492/ijcce.2024.2018739.6368
19. S.A. Saoud, K.F. Ali and R.M. Shakir, Relationship Between the structure of Newly Synthesized derivatives of 1,3,4-oxadiazole Containing 2-Methylphenol and their Antioxidant and Antibacterial Activities, *Orient. J. Chem*., 2017, **33**, no. 4, 1781. doi: 10.13005/ojc/330423
20. F.J. Giessible, Advances in atomic force microscope, *Rev. Mod. Phys*., 2003, **75**, no. 3, 949–983. doi: 10.1103/RevModPhys.75.949
21. M.D. Hanwell, D.E. Curtis, D.C. Lonie, T. Vandermeersch, E. Zurek and G.R. Hutchison, Avogadro: an advanced semantic chemical editor, visualization, and analysis platform, *J. Cheminform*., 2012, **4**, 1–17. doi: 10.1186/1758-2946-4-17
22. N.M. O'Boyle, Open Babel: An open chemical toolbox, *Journal of cheminformatics*, 2011, **3**, 1–14.
23. G.M. Morris, R. Huey, W. Lindstrom, M.F. Sanner, R.K. Belew, D.S. Goodsell and A.J. Olson, AutoDock4 and AutoDockTools4: Automated docking with selective receptor flexibility, *J. Comput. Chem*., 2009, **30**, no. 16, 2785–2791. doi: 10.1002/jcc.21256
24. Y. Liu, X. Yang, J. Gan, S. Chen, Z.-X. Xiao and Y. Cao, CB-Dock2: improved protein–ligand blind docking by integrating cavity detection, docking and homologous template fitting, *Nucleic Acids Res*., 2022, **50**, W159–W164. doi: 10.1093/nar/gkac394

25. E.F. Pettersen, T.D. Goddard, C.C. Huang, E.C. Meng, G.S. Couch, T.I. Croll, J.H. Morris and T.E. Ferrin, UCSF ChimeraX: Structure visualization for researchers, educators, and developers, *Protein Sci*., 2021, **30**, no. 1, 70–82. doi: 10.1002/pro.3943
26. R.M. Shakir, Synthesis, antioxidant activity and molecular docking study of 1,2,4-Triazole and their corresponding fused rings containing 2-Methylphenol, *Int. J. Drug Deliv. Technol*., 2021, **11**, no. 2, 501–511. doi: 10.25258/ijddt.11.2.47
27. R.M. Shakir, Synthesis, Antioxidant, antibacterial and docking structure of new dihydro-pyrimidine derivatives containing multi phenol, *J. Pharm. Negat. Results*, 2022, **13**, no. 2, 57–68. doi: 10.47750/pnr.2022.13.02.009
28. N.A. Hikmat and S.A. Mahmood, *Comparispon study on corrosion protectiveness of nanostructured electropolymerized polyaniline derivitives*, 2015, M.Sc. Thesis, College of science, University of Baghdad
29. S.A. Kumar, A. Sankar and S.R. Kumar, Vitamin B-12 Solution as Corrosion Inhibitor for Mild Steel in Acid Medium, *Int. J. Comput. Eng. Sci*., 2013, **3**, no. 1, 57–61.
30. K.A. Saleh and S.A. Habeeb, Electrochemical Polymerization and Biological Activity of 4-(Nicotinamido)-4-Oxo-2-Butenoic Acid as An Anticorrosion Coatingon A 316L Stainless Steel Surface, *Iraqi J. Sci*., 2021, **62**, no. 3, 729–741. doi: 10.24996/ijs.2021.62.3.3
31. I. Nadi, Z. Belattmania, B. Sabour, A. Reani, A. Sahibed-Dine, C. Jama and F. Bentiss, *Sargassum muticum* extract based on alginate biopolymer as a new efficient biological corrosion inhibitor for carbon steel in hydrochloric acid pickling environment: Gravimetric, electrochemical and surface studies, *Int. J. Bio. Mac*., 2019, **141**, 137–149. 10.1016/j.ijbiomac.2019.08.253
32. M. Lorenzetti, E. Pellicer, J. Sort, M.D. Baró, J. Kovač, S. Novak, and S. Kobe, Improvement to the Corrosion Resistance of Ti-Based Implants Using Hydrothermally Synthesized Nanostructured Anatase Coatings, *Materials*, 2014, **7**, no. 1, 180–194. doi: 10.3390/ma7010180
33. H.A. Almashhadani, Using expired pharmaceutical Clotrimazole as a corrosion inhibitor for stainless steel in acidic media, *Int. J. Corros. Scale Inhib*., 2024, **13**, no, 3, 1636–1648. doi: 10.17675/2305-6894-2024-13-3-15
34. A.A. Alamiery, Synthesized Heterocyclic Compounds as Corrosion Inhibitors for Steel in Acidic Environments: A Mini-Review, *J. Mater. Eng*., 2024, **2**, no. 4, 235–249. doi: 10.61552/JME.2024.04.001
35. A. Narayanswamy, D. Ramakrishna, P.V.R. Shekar, S. Rajendrachari and R. Sudhakar, Quantum Chemical and Experimental Evaluation of a 4-AminoAntipyrine Based Schiff Base as Corrosion Inhibitor for Steel Materia, *ACS Omega*, 2024, **9**, 13262−13273. doi: 10.1021/acsomega.3c10048
36. H.A. Almashhadani, Synthesis of a CoO-ZnO nanocomposite and its study as a corrosion protection coating for stainless steel in saline solution, *Int. J. Corros. Scale Inhib*., 2021, **10**, no. 3, 1294–1306. doi: 10.17675/2305-6894-2021-10-3-26

37. M.A. Amin, S.S.A.El Rehim and H.T.M. Abdel-Fatah, Electrochemical frequency modulation and inductively coupled plasma atomic emission spectroscopy methods for monitoring corrosion rates and inhibition of low alloy steel corrosion in HCl solutions and a test for validity of the Tafel extrapolation method, *Corros. Sci*., 2009, **51**, no. 4, 882–894. doi: 10.1016/j.corsci.2009.01.006
38. F. Bentiss, B. Mernari, M. Traisnel, H. Vezin and M. Lagrenée, On the relationship between corrosion inhibiting effect and molecular structure of 2,5-bis(*n*-pyridyl)-1,3,4-thiadiazole derivatives in acidic media: Ac impedance and DFT studies, *Corros. Sci*., 2011, **53**, no. 1, 487–495. doi: 10.1016/j.corsci.2010.09.063
39. S. Banerjee, V. Srivastava and M.M. Singh, Chemically modified natural polysaccharide as green corrosion inhibitor for mild steel in acidic medium, *Corros. Sci*., 2012, **59**, 35–41. doi: 10.1016/j.corsci.2012.02.009
40. A. Umoren, I.B. Obot, E.E. Ebenso, N.O. Obi-Egbedi, The Inhibition of aluminium corrosion in hydrochloric acid solution by exudate gum from *Raphia hookeri*, *Desalination*, 2009, **247**, no. 1–3, 561–572. doi: 10.1016/j.desal.2008.09.005
41. M.G. Fontana, N.D. Greene and J. Klerer, Corrosion Engineering, *J. Electrochem. Soc*., 1968, **115**, 142C.
42. E.A. Noor and A.H. Al-Moubaraki, Thermodynamic study of metal corrosion and inhibitor adsorption processes in mild steel/1-methyl-4[4′(-X)-styryl pyridinium iodides/hydrochloric acid systems, *Mater. Chem. Phys*., 2008, **110**, no. 1, 145–154. doi: 10.1016/j.matchemphys.2008.01.028
43. S.A. Habeeb, H.A. Almashhadani, Synthesis of polysulfanilamide by electro polymerization and its corrosion protective properties on 316L stainless steel in 0.2 M HCl. *Int. J. Corros. Scale Inhib*., 2022, **11**, no. 2, 621–32. doi: 10.17675/2305-6894-2022-11-2-11
44. H. Hochegger, S. Takeda and T. Hunt, Cyclin-dependent kinases and cell-cycle transitions: does one fit all? *Nat. Rev. Mol. Cell Biol*., 2008, **9**, no. 11, 910–916. doi: 10.1038/nrm2510
45. J.I. Trujillo, J.R. Kiefer, W. Huang, A. Thorarensen, L. Xing, N.L. Caspers, J.E. Day, K.J. Mathis, K.K. Kretzmer and B.A. Reitz, 2-(6-Phenyl-1*H*-indazol-3-yl)-1*H*-benzo [d] imidazoles: Design and synthesis of a potent and isoform selective PKC-ζ inhibitor, *Bioorg. Med. Chem. Lett*., 2009, **19**, no. 3, 908–911. doi: 10.1016/j.bmcl.2008.11.105
46. S. Tadesse, E.C. Caldon, W. Tilley, S. Wang, Cyclin-dependent kinase 2 inhibitors in cancer therapy: an update, *J. Med. Chem*., 2018, **62**, no. 9, 4233–4251. doi: 10.1021/acs.jmedchem.8b01469
47. H. Liang, Y. Zhu, Z. Zhao, J. Du, X. Yang, H. Fang and X. Hou, Structure-based design of 2-aminopurine derivatives as CDK2 inhibitors for triple-negative breast cancer, *Front. Pharmacol*., 2022, **13**, 864342. doi: 10.3389/fphar.2022.864342
48. H.T. Abdel-Mohsen, Oxindole–benzothiazole hybrids as CDK2 inhibitors and anticancer agents: design, synthesis and biological evaluation, *BMC Chem*., 2024, **18**, no. 1, 169. doi: 10.1186/s13065-024-01277-1

49. M.S. Raied, A.S. Shaimaa, F.H. Dhuha, F.A. Khalid, S.A. Firas and S.J. Husam, Synthesis, Antioxidant ability and Docking study for new 4,4′-((2-(Aryl)-1*H*-benzo[d]imidazole-1,3(2*H*)-diyl)bis(methylene))diphenol, *Res. J. Chem. Environ.*, 2022, **26**, no. 10, 28–36. doi: 10.25303/2610rjce028036
50. Y. Li, J. Zhang, W. Gao, L. Zhang, Y. Pan, S. Zhang and Y. Wang, Insights on structural characteristics and ligand binding mechanisms of CDK2, *Int. J. Mol. Sci*., 2015, **16**, no. 5, 9314–9340. doi: 10.3390/ijms16059314

♦ ♦ ♦